

Capillary waves in miscible fluids

Alessandro Carbonaro,¹ Giovanni Savorana,^{1,*} Luca Cipelletti,^{1,2} Rama Govindarajan,³ and Domenico Truzzolillo^{1,†}

¹*Laboratoire Charles Coulomb (L2C), UMR 5221 CNRS-Université de Montpellier, F-34095 Montpellier, France*

²*Institut Universitaire de France, F-75231 Paris, France*

³*International Centre for Theoretical Sciences, Tata Institute of Fundamental Research, Shivakote, Bengaluru 560089, India*

(Dated: September 30, 2024)

We report the existence of capillary waves propagating along the boundary between miscible co-flowing fluids. We unveil that the interplay between transient interfacial stresses and confinement drives the progressive transition from the well-known inertial regime, characterized by a wavenumber independent of frequency, $k \sim \omega^0$, to an unexpected capillary-wave scaling, $k \sim \omega^{2/3}$. This allows us to measure the effective interfacial tension between miscible fluids and its rapid decay on time scales never probed so far, which we rationalize with a model going beyond square gradient theories.

Capillary waves are small disturbances propagating on the interface between two fluids, with such a short wavelength that the only restoring force effectively at work is interfacial tension [1–3]. They are very common in Nature [1] but they can also be easily produced artificially [4, 5]. Notably, capillary waves have proved to be a valuable tool to measure interfacial or surface tension between immiscible fluids [6], since their dispersion relation links the tension Γ to the wavenumber k and frequency ω of the waves. Recently, Hu and Cubaud [7] have shown that propagating modes can be excited in viscosity-stratified flows confined in microfluidic channels, and that some of the waves observed for coflowing immiscible liquids follow the capillary wave dispersion predicted for inviscid fluids, with a scaling $k \sim \omega^{2/3}$ [1]. Hence, even in confined flows, capillary waves can emerge when interfacial tension dominates over other stabilizing mechanisms such as viscous dissipation. In the flow of miscible fluids interfacial stresses, whose very existence is being debated by an increasing number of research groups in recent years [8–13], are typically negligible compared to viscous dissipation. An “inertial” regime characterizes the emerging instability, with $k \sim \omega^0$ [7]: the variation of the wave frequency is solely dictated by a change in phase velocity, while the wavelength stays practically unaltered when the flow rate of either fluid is varied. This regime has been also observed for high Reynolds numbers in immiscible fluids, where it delimits the short wavelength limit [7] of the stability diagram, suggesting a maximum wavenumber dictated only by the rate of energy dissipation of the waves. Hence, dissipation, confinement and interfacial tension are key to understand the observed instability and the transition from the inertial to the capillary regime.

Capillary waves in miscible fluids have not been reported so far, most likely due to the rapidly decaying tension at their boundaries [9, 14–18]. However, since

wave formation at the interface between coflowing liquids in microfluidic devices can be a very fast process, with just a few tens of milliseconds elapsing from the first contact between fluids to the instability occurrence, microfluidics provides an ideal playground to test whether interfacial stresses due to large concentration gradients can transiently impact wave propagation. In this letter, we investigate in detail the propagation of shear flow instabilities appearing when water and glycerol flow side-by-side in rectangular microchannels. We unveil the existence of capillary waves in miscible co-flowing liquids, two distinct branches of wave dispersion, and, from the analysis of wave propagation in space, we measure the effective interfacial tension at the liquid-liquid boundary over time scales never probed so far.

We generated and visualized interfacial waves by pumping deionized water and glycerol in polydimethylsiloxane (PDMS) microchannels, as sketched in Fig. 1 (a) ([19]). Most of the experiments and the detailed analysis of wave propagation have been carried out in a channel whose main duct has height $H = 0.1$ mm and width $W = 1$ mm. Further experiments to inspect the role of lateral confinement have been performed in a narrower channel, $W = 0.25$ mm, with the same height and Y-geometry. The two fluids flow parallel to each other and the interface is vertical, parallel to the gravity direction \hat{z} , thus ruling out any effect due to density mismatch, at least in the first portion of the channel, where the two fluids stay in parallel co-flow and do not re-orient themselves to minimize gravitational energy.

The instability is observed via optical microscopy at its onset, and it is characterized by recording the interface dynamics at fixed flow rate of glycerol Q_G and varying the flow rate of water from $Q_H = 0$ $\mu\text{l}/\text{min}$ to several hundreds of $\mu\text{l}/\text{min}$, depending on Q_G . We repeated this protocol in the range $3\mu\text{l}/\text{min} \leq Q_G \leq 25\mu\text{l}/\text{min}$. The instability appears above a critical flow rate of water Q_{H2O}^c that depends marginally on Q_G ([19]). The typical base flow is sketched in Fig. 1-b, with water being the faster moving fluid. The velocity profiles in absence of diffusion change curvature at the interface, located at $y = Y$. This configuration allows to link the stream wise position ΔX of the instability onset and the diffusion

* Currently at Institute of Environmental Engineering, ETH Zurich, 8093, Zurich, Switzerland

† domenico.truzzolillo@umontpellier.fr

time t_c , since $t_c = \Delta X/U(Y, H/2)$, where $U(Y, H/2)$ is the base flow velocity of the interface at the imaged plane $z = H/2$.

As shown in Figs 1 (c,d), the interface can be visualized thanks to the large difference in refractive index at $T=25^\circ\text{C}$ between water ($n = 1.333$) and glycerol ($n = 1.472$). Here, both the fluids flow from left to right, with glycerol occupying the upper part of the channel. The shape of the wave front in each frame is reconstructed by tracking the position Y of the interface in the direction orthogonal to the flow direction, \hat{x} , thus obtaining a curve in the $x - y$ plane that closely represents the contour of the deformed interface ([19]). The spatio-temporal averages and the respective standard deviations of the wavelength, the phase velocity in the laboratory frame and the amplitude are directly extracted from image analysis ([19]).

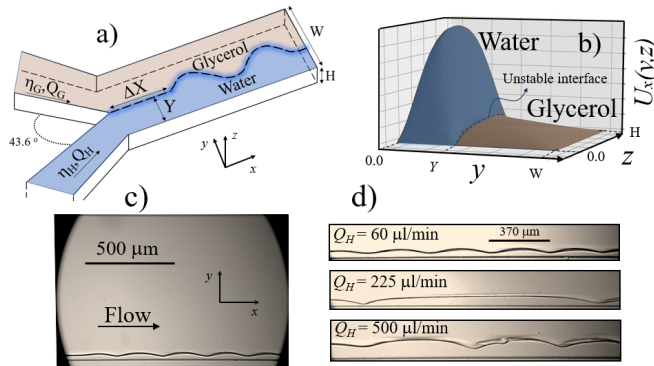


FIG. 1. Experimental setup and flow configuration. **a**: Scheme of the Y-junction chip used to generate co-flowing fluids. **b**: Characteristic 3D-base flow for water and glycerol in the main duct. **c**: Entire field of view for $(Q_G, Q_H) = (18 \mu\text{l}/\text{min}, 60 \mu\text{l}/\text{min})$ and $W = 1\text{mm}$. **d**: Interfacial instabilities observed for three different flow rates of water at $Q_G = 18 \mu\text{l}/\text{min}$. Note that $\lambda(Q_H)$ is non-monotonic.

Figure 1-(c) and (d) set the scene for describing the general phenomenology of the observed co-flow instabilities. In (c) we show the entire field of view for one single set of flow rates. The instability develops close to the wall at $y = 0$. This is always the case in our experiments since the unperturbed interface stays in the range $30 \mu\text{m} \leq Y \leq 320 \mu\text{m}$. In (d) we show three frames depicting the emerging instability at three selected flow rates of water for the same $Q_G = 18 \mu\text{l}/\text{min}$. Remarkably, the wavelength of the instability does not vary monotonically upon increasing Q_H : the average wavelength λ of the instability first increases with Q_H , reaching very large values (up to $\lambda > W$) for intermediate Q_H , and finally declines when the water rate is increased further. In none of the cases we observe a spatio-temporal evolution of the instability amplitude in the accessible field of view (1.6 mm downstream of the onset): almost instantaneously the observed waves reach a steady amplitude, pointing to a non-linear saturation in the instability production with mode-coupling at play [20]. This has been already underlined in [7] for other pairs of fluids.

Figures 2-a,b show the result of our image analysis for the wavelength λ and the phase velocity of the waves in the frame of the unperturbed interface, $v_{ph} = v_{ph}^{lab} - U(Y, H/2)$, with $U(Y, H/2)$ computed analytically or retrieved from the interface position ([19]). Note that the subtraction of the base flow velocity at $y = Y$ is necessary to get rid of a Doppler shift caused by the underlying fluid motion [21, 22]. However, we emphasize that our results do not qualitatively change if this subtraction is not considered, as in [7]. As suggested by Fig 1-d the instability wavelength develops a maximum, which grows in magnitude and shifts to higher rates of water for increasing rate of glycerol, Fig. 2-a. By contrast, the phase velocity increases sharply right above the critical rate of water Q_H^c for the instability (Fig. 2-(b) and [19]), and then becomes very weakly dependent on the water flow rate. This occurs for all the investigated Q_G . Similarly to the phase velocity, the amplitude of the instability exhibits two regimes with a rapid increase followed by nearly constant plateau as a function of Q_H ([19]). Quite generally, Q_G determines a systematic increase of the wavelength, the phase velocity and the amplitude ([19]) at any $Q_H > Q_H^c$.

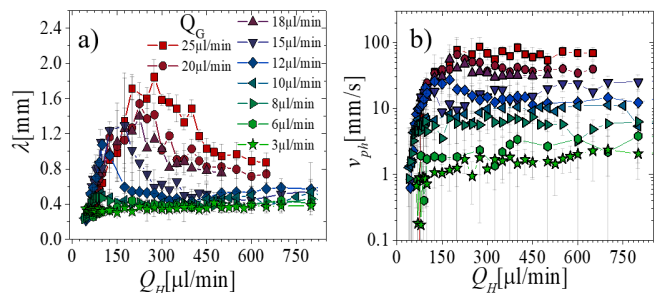


FIG. 2. Wavelength λ (**a**) and phase velocity v_{ph} (**b**) of the observed interfacial waves as a function of the flow rate of water Q_H , for different flow rates of glycerol as indicated in panel **a**. The color code and symbol type are the same for both panels. Error bars are spatio-temporal standard deviations ([19]).

Figure 3 shows the dispersion relation $\omega(k) = v_{ph}(k)k$ of the waves, with $k = 2\pi/\lambda$. It is characterized by the presence of two distinct branches for all rates of glycerol for which $\lambda(Q_H)$ is non-monotonic. One can distinguish a first branch, which we call *C*-branch, corresponding to the highest rates of water, where the frequency increases with increasing k , and a second branch, that we call *CD*, where the frequency decreases with k at high Q_G , becoming almost k -independent and eventually limited over a very small range of k as Q_G is decreased down to $3 \mu\text{l}/\text{min}$ (*D*-waves), where the *C*-branch is absent. For the sake of clarity a stability diagram in the $Q_G - Q_H$ plane, including *C*, *CD* and *D* waves, is reported in [19]. Here, *C*, *CD* and *D* stand for capillary, capillary-dissipative and dissipative respectively, as discussed later.

The *C*-branch is strongly reminiscent of the capillary dispersion observed in immiscible co-flowing liquids [7]

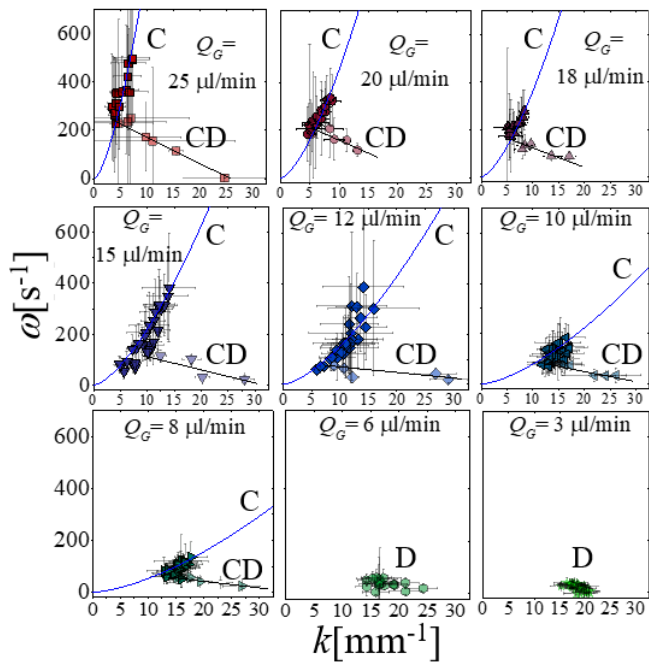


FIG. 3. Dispersion relation for all Q_G from the highest rate (25 $\mu\text{l}/\text{min}$) to the lowest (3 $\mu\text{l}/\text{min}$). Blue lines are the fit of the C-branch with a capillary wave scaling $\omega = \alpha k^{3/2}$, see text for details. The C-branch vanishes for $Q_G < 8 \mu\text{l}/\text{min}$.

and we have thus inspected further this branch, that is indeed well fitted by a capillary wave-type dispersion [1] (blue lines in Fig. 3):

$$\omega = \alpha k^{3/2} \quad (1)$$

with α that decreases for decreasing Q_G , until when the C-branch vanishes and only D-waves remain. This scenario is quite surprising since capillary waves in confined shear flows were reported only for immiscible fluids, while miscible ones only showed an inertial regime with a wavenumber independent of frequency [7]. To validate our fitting procedure we report in Fig. 4-a the wavenumber vs the rescaled frequency ω/α and we fit the entire set of points belonging to the C-branches with a power-law $k = C_0(\omega/\alpha)^\beta$. We obtain $\beta = 0.67 \pm 0.05$ in very good agreement with the expected capillary wave scaling $\beta_c = 2/3$ [1]. From the best fit of eq. 1 to the C-branches we computed the effective tension between water and glycerol for each Q_G , using the known relationship $\alpha = [\Gamma_e/(\rho_H + \rho_G)]^{1/2}$, where ρ_H and ρ_G are the densities of water and glycerol, respectively [1, 7].

Figure 4-b shows Γ_e as a function of the average time $t_c = \Delta X/\langle v_{int} \rangle$ that the two fluids spend side-by-side until the instability takes place, where $\langle v_{int} \rangle$ is the unperturbed speed of the interface averaged over the rates Q_H belonging to the C-branch. Note that this averaging is sound, since the speed of the interface depends mainly on Q_G and only very marginally on Q_H ([19]). Together with the values extracted from the

present analysis of wave propagation, we report also Γ_e as from the deformation of spinning droplets of water in a reservoir of glycerol 15 s after the first contact between the fluids. The effective interfacial tension shows a very rapid decrease for increasing contact time going from 2.3 mN/m at $t_c = 61$ ms down to 6.3 $\mu\text{N}/\text{m}$ at $t_c = 0.17$ s, decaying way faster than the $\Gamma_e \sim t_c^{-1/2}$ scaling predicted for small gradients, where the square gradient (SG) expansion of the free energy is supposed to hold [17, 23]. The values that we obtain are in stark contrast with spinning drop tensiometry data reported previously for the same liquids: in [23] $\Gamma_e = 0.58$ mN/m after about hundred of seconds from contact, a result leveraging on the assumption that water droplets spinning in a reservoir of glycerol evolve through a series of quasi-equilibrated states during their continuous elongation. The present results question this assumption and call for a different explanation.

We find that our entire set of data, including the one measured in [24], are very well fitted (Fig. 4-b) by a model that some of us developed in [9], where higher order terms in the gradient expansion of the free energy are taken into account. The full expression for Γ_e reads

$$\Gamma_e(t_c) = \Gamma_{SG} + \Gamma_0 \left[\cosh\left(\frac{L}{\delta(t_c)}\right) - \frac{L^2}{2\delta^2(t_c)} - 1 \right], \quad (2)$$

where Γ_{SG} is the square gradient contribution to the tension, that can be computed on-lattice for molecular fluids [24]:

$$\Gamma_{SG} = \frac{RTa^2}{V_m\delta(t_c)} \left(\frac{2}{3} + \frac{\chi_{wg}}{6} \right) \quad (3)$$

where R is the ideal gas constant, $a = 0.45$ nm and $V_m = 45.5$ ml/mol are the average diameter and the average molar volume of the fluid molecules, respectively, and $\chi_{wg} = -0.96$ is the Flory interaction parameter for water and glycerol [9]. $\Gamma_0 = \varepsilon\delta(t_c)$ sets the scale of the contribution to the effective tension due to large gradients at short times, via the energy density ε and the interface thickness $\delta(t_c)$. L is a characteristic length setting the thickness below which higher order terms in the free energy gradient expansion starts affecting the tension. We further assume that the interface thickness $\delta(t_c)$ increases in time due only to transverse diffusion, $\delta(t_c) = \sqrt{2D_{wg}t_c}$, with $D_{wg} = 1.4 \times 10^{-11} \text{m}^2/\text{s}$ the diffusion coefficient of water in glycerol [24, 25]. Equation 2 therefore contains only 2 free fitting parameters, L and ε , for which we obtain $L = 26.5 \pm 3.5 \mu\text{m}$ and $\varepsilon = (43 \pm 24) \times 10^{-6}$ Pa.

Quite intriguingly, if we assume that the energy density ε is dominated by excluded volume interactions and that local equilibrium [26] may be invoked to use fluctuation-dissipation scaling as crude approximation to estimate the correlation length associated to this density, we obtain $l_D = (k_B T/\varepsilon)^{1/3} = 4.54 \pm 0.84 \mu\text{m}$, i.e. a value of the same order of magnitude of the interface thickness

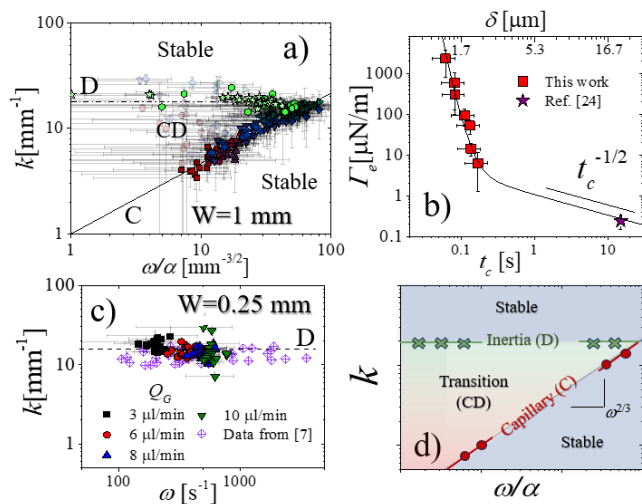


FIG. 4. **a**: Dispersion relation k vs scaled frequency ω/α for the waves observed in the widest channel ($W = 1$ mm). Same color code as in Fig. 1. The shadowed points are those belonging to the CD -branches observed for those Q_G where the C -branch exists, and where the amplitude depends on the interface position ([19]). The solid line is the best power-law fit to the C -branch, $k = C_0(\omega/\alpha)^{0.67 \pm 0.05}$. The dashed horizontal line marks the average value of the wave number, $k_D = 18 \text{ mm}^{-1}$, obtained by averaging the data for $Q_G = 6 \mu\text{l}$ and $Q_G = 3 \mu\text{l}$. **b**: Effective interfacial tension Γ_e vs time elapsed from contact t_c (bottom axis) and interface thickness (top axis). The solid line is the best fit obtained via Eq. 2. **c**: Dispersion relation k vs ω for the waves observed in the narrowest channel ($W = 0.25$ mm). **d**: Sketch of the general stability diagram proposed for shear flow instabilities at the boundary between 2 liquids in microfluidic flows, with the capillary branch and the inertial regime delimiting the instability region.

in our experiments, marking the transition between the nearly-exponential decay of the tension and the square gradient scaling. Moreover, l_D is lower than L , in analogy to previous findings for colloidal and polymeric fluids [9]. In this respect it has been argued [27–30] that the emergence of a characteristic length larger than typical structural length scales is a consequence of a system being strongly driven as observed in a variety of systems, from flowing granular matter, to colloidal and polymer systems. We also note that the steep exponential-like decay of the tension observed for small t_c is reminiscent of the steep decay of the tension found in [16] for static conditions and near-critical fluids. Our fit suggests therefore the existence of two distinct decay regimes for interfacial stresses at miscible liquid/liquid boundaries: at short time scales, sharp gradients relax and high-order terms in the free-energy gradient expansion dominate over the square gradient term. At large time scales, by contrast, the concentration gradients are small and the SG term dominates: its contribution is necessary to account for the point that we obtained analyzing spinning drop deformations at large t_c (star in Fig 4-b).

We make further use of the best fit (Eq. 2) and from the experimental t_c we compute the effective tension for those rates of glycerol for which we do not observe the C -branch. We obtain $\Gamma_e = 2.97 \mu\text{N/m}$ and $1.78 \mu\text{N/m}$ for $Q_{Gly} = 6$ and $3 \mu\text{l/min}$, respectively. We used these values to compute the prefactor α (Eq.1) and report the wavenumber as a function of the rescaled frequency ω/α also for the two lowest Q_G (green symbols in Fig. 4-a). Remarkably, we find that the wavenumber does not show any clear dependence over almost 2 decades in frequency (full range shown in [19]), scattering around an average value $k_D = 18 \pm 2 \text{ mm}^{-1}$, and merging to the highest wavenumber region of the capillary branch, akin to what has been observed in [7] for a silicone oil and ethanol, a pair of immiscible fluids with a viscosity contrast similar to glycerol and water (see [19] for a direct comparison).

Our results, in contrast with those reported in [7], thus suggest two different mechanisms driving wave propagation at the boundary between miscible fluids, giving rise to two distinct branches of the wave dispersion. One of them is characterized by the same inertial scaling, the D -branch here, observed in [7], while the other (the C -branch) and the apparent transition between them (the CD regime) are observed in the present work and are absent in [7]. This discrepancy requires a further inspection.

We note that our experiments have been performed in a channel ($W = 1 \text{ mm}$) wider than that of [7] ($W = 0.25 \text{ mm}$). We therefore start inquiring whether confinement is key for the appearance of waves following the inertial scaling $k \sim \omega^0$ or, in other words, whether confinement hampers the capillary regime $k \sim \omega^{2/3}$. We have performed further co-flow experiments employing a narrower channel, $W = 0.25 \text{ mm}$, in the same range of Reynolds numbers ([19]). Notably, we did not observe the onset of a capillary branch in the dispersion relation, consistently with the results of [7] for miscible fluids (Fig. 4-c). For the narrow channel, our data and those of ref. [7] are indeed in excellent quantitative agreement as shown in Fig. 4-c. A further clue of the key role played by confinement is given by the fact that the transition from C to CD waves occurs when the the interface position Y becomes equal to the wave amplitude ([19]), which sharply decreases by approaching further the wall at $y = 0$. We conclude that lateral confinement is responsible for suppressing capillary waves under weak tensions and we propose that the mode selection in this case is driven by a minimum-dissipation principle dictating the minimum wavelength emerging for this instability, as it occurs for other instabilities where the capillary stresses at play are very low [31]. It is not surprising therefore that, what have been called inertial regime, defines the upper bound of the unstable region in Fig. 4-a and for the experimental results reported in [7]. Once established the existence of these two kinds of waves in confined co-flows, the CD -regime observed for $Q_G \geq 8 \mu\text{l/l}$ that is characterized by the departure from pure capillary (C)

branch towards the inertial one, can be ascribed to the competition between the two modes (C and D). We consider therefore that this is a transition region in a very general stability diagram, as sketched in Fig. 4-d. As a final remark, we emphasize that the same two branches (C and D) delimiting the instability region of the diagram appear in both miscible and immiscible fluids, as shown in Fig. SM7 in [19]. The overlap of the wave dispersions observed in pairs of immiscible and fully miscible fluids support further the importance of interfacial stresses at diffuse interfaces far from equilibrium.

In this letter we reported the existence of waves that emerge spontaneously at the interface between miscible liquids in viscosity-stratified microfluidic flows, following two types of dispersive behavior. Wave propagation is dominated respectively by interfacial stresses for high flow rates and large concentration gradients (C -branch), while dissipation and confinement dominate in the inertial regime, where one single wavenumber emerges. The transition from capillary waves to the inertial regime is generally smooth and occurs when the rate of the fastest fluid is decreased so that diffusion smears out interfaces, interfacial stresses become vanishingly small, and waves get concomitantly more confined. We found very good agreement between the measured values of the effective

tension and a model [9] that goes beyond the well-known second order gradient expansion of pressures and mixing free energy in systems far from equilibrium [14, 32]. Our results indicate that interfacial tension in miscible molecular fluids decay much faster right after contact than the temporal decay predicted by square gradient models $\Gamma_e \sim t^{-1/2}$, as suggested by other results in static conditions [16], while the square gradient approximation holds at later stages [24]. Capillary waves observed in microfluidic flows of miscible liquids are a novel and unexpected phenomenon, that is put forward as a probe for tensions with unique properties, where steady wave patterns give access to stresses over the millisecond scale after the first liquid-liquid contact, thus paving the way for a thorough understanding of capillary phenomena and flow stability in miscible fluids.

ACKNOWLEDGMENTS

DT warmly thanks Prof. Laura Casanellas for help in manufacturing the microchannels. LC gratefully acknowledges support from the Institut Universitaire de France (IUF). We gratefully acknowledge support from the Centre national d'études spatiales (CNES).

-
- [1] H. Lamb, *Hydrodynamics*, 6th ed. (Cambridge University Press., New York, 1932).
 - [2] Rayleigh, On Progressive Waves, Proceedings of the London Mathematical Society **s1-9**, 21 (1877).
 - [3] T. Chou, S. K. Lucas, and H. A. Stone, Capillary wave scattering from a surfactant domain, *Physics of Fluids* **7**, 1872 (1995).
 - [4] L. C. Bobb, G. Ferguson, and M. Rankin, Capillary wave measurements, *Appl. Opt.* **18**, 1167 (1979).
 - [5] F. Behroozi, B. Lambert, and B. Buhrow, Direct measurement of the attenuation of capillary waves by laser interferometry: Noncontact determination of viscosity, *Appl. Phys. Lett.* **78**, 2399 (2001).
 - [6] C. H. Sohl, K. Miyano, and J. B. Ketterson, Novel technique for dynamic surface tension and viscosity measurements at liquid-gas interfaces, *Review of Scientific Instruments* **49**, 1464 (1978).
 - [7] X. Hu and T. Cubaud, Viscous Wave Breaking and Ligament Formation in Microfluidic Systems, *Phys. Rev. Lett.* **121**, 044502 (2018).
 - [8] M. Bier, Nonequilibrium interfacial tension during relaxation, *Phys. Rev. E* **92**, 042128 (2015).
 - [9] D. Truzzolillo, S. Mora, C. Dupas, and L. Cipelletti, Nonequilibrium Interfacial Tension in Simple and Complex Fluids, *Phys. Rev. X* **6**, 041057 (2016).
 - [10] R. X. Suzuki, F. W. Quah, T. Ban, M. Mishra, and Y. Nagatsu, Experimental study of miscible viscous fingering with different effective interfacial tension, *AIP Advances* **10**, 115219 (2020).
 - [11] V. K. Gowda, C. Rydefalk, L. D. Söderberg, and F. Lundell, Formation of colloidal threads in geometrically varying flow-focusing channels, *Phys. Rev. Fluids* **6**, 114001 (2021).
 - [12] A. Vorobev, S. Prokopev, and T. Lyubimova, Nonequilibrium Capillary Pressure of a Miscible Meniscus, *Langmuir* **37**, 4817 (2021).
 - [13] L. Lacaze, P. Guenoun, D. N. Beysens, M. Delsanti, P. Petitjeans, and P. Kurovski, Transient surface tension in miscible liquids, *Physical Review E* **82**, 041606 (2010).
 - [14] D. Korteweg, Sur la forme que prennent les équations du mouvements des fluides si l'on tient compte des forces capillaires causées par des variations de densité considérables mais connues et sur la théorie de la capillarité dans l'hypothèse d'une variation continue de la densité, *Arch. Neerland. Sci. Exact. et Naturell.* **6**, 1 (1901).
 - [15] J. A. Pojman, C. Whitmore, M. L. Turco Liveri, R. Lombardo, J. Marszalek, R. Parker, and B. Zoltowski, Evidence for the Existence of an Effective Interfacial Tension between Miscible Fluids: Isobutyric Acid-Water and 1-Butanol-Water in a Spinning-Drop Tensiometer, *Langmuir* **22**, 2569 (2006).
 - [16] P. Cicuta, A. Vailati, and M. Giglio, Capillary-to-bulk crossover of nonequilibrium fluctuations in the free diffusion of a near-critical binary liquid mixture, *Applied Optics* **40**, 4140 (2001).
 - [17] P. Smith, T. Van De Ven, and S. Mason, The transient interfacial tension between two miscible fluids, *Journal of Colloid and Interface Science* **80**, 302 (1981).
 - [18] D. Truzzolillo, S. Mora, C. Dupas, and L. Cipelletti, Off-Equilibrium Surface Tension in Colloidal Suspensions, *Physical Review Letters* **112**, 128303 (2014).
 - [19] See Supplemental Material at [URL will be inserted by publisher] for I) Fabrication of the microchannels;

- II) Visualization and tracking of the waves; III) Low-Reynolds-number instabilities; IV) Base flow profile of two co-flowing fluids in a rectangular channel; V) Accuracy of the interface position and interfacial velocity of the unperturbed interface; VI) Wave amplitude, confinement and critical rates of water VII) Stability diagram; VIII) Comparison between miscible and immiscible fluids (Data from [7]).
- [20] L. D. Landau and E. M. Lifshitz, *Course of Theoretical Physics, Volume 6 - Fluid Mechanics*. (Pergamon Press, 1987).
- [21] F. Denner and B. G. Van Wachem, Numerical time-step restrictions as a result of capillary waves, *Journal of Computational Physics* **285**, 24 (2015).
- [22] G. Giamagas, F. Zonta, A. Roccon, and A. Soldati, Propagation of capillary waves in two-layer oil–water turbulent flow, *J. Fluid Mech.* **960**, A5 (2023).
- [23] P. Petitjeans, Petitjean - Une tension de surface pour les fluides miscibles, *C.R. Acad. Sci. Paris* , 673 (1996).
- [24] A. Carbonaro, L. Cipelletti, and D. Truzzolillo, Ultralow effective interfacial tension between miscible molecular fluids, *Phys. Rev. Fluids* **5**, 074001 (2020).
- [25] G. D’Errico, O. Ortona, F. Capuano, and V. Vitagliano, Diffusion Coefficients for the Binary System Glycerol + Water at 25 °C. A Velocity Correlation Study, *Journal of Chemical & Engineering Data* **49**, 1665 (2004).
- [26] S. Kjelstrup and D. Bedeaux, *Non-Equilibrium Thermodynamics of Heterogeneous Systems*, Series on Advances in Statistical Mechanics No. Volume 16 (World Scientific, Singapore, 2008).
- [27] J. A. G. Orza, R. Brito, T. P. C. Van Noije, and M. H. Ernst, Patterns and Long Range Correlations in Idealized Granular Flows, *Int. J. Mod. Phys. C* **08**, 953 (1997), arXiv:cond-mat/9702029.
- [28] É. Guazzelli and J. Hinch, Fluctuations and Instability in Sedimentation, *Annu. Rev. Fluid Mech.* **43**, 97 (2011).
- [29] H. Katsuragi, A. R. Abate, and D. J. Durian, Jamming and growth of dynamical heterogeneities versus depth for granular heap flow, *Soft Matter* **6**, 3023 (2010).
- [30] X.-L. Wu, D. J. Pine, and P. K. Dixon, Enhanced concentration fluctuations in polymer solutions under shear flow, *Phys. Rev. Lett.* **66**, 2408 (1991).
- [31] L. Paterson, Fingering with miscible fluids in a Hele Shaw cell, *Physics of Fluids* **28**, 26 (1985).
- [32] I. Roušar and E. Nauman, A continuum analysis of surface tension in nonequilibrium systems, *Chemical Engineering Communications* **129**, 19 (1994).

Supplemental Material: Capillary waves in miscible fluids

Alessandro Carbonaro,¹ Giovanni Savorana,^{1,*} Luca
Cipelletti,^{1,2} Rama Govindarajan,³ and Domenico Truzzolillo^{1,†}

¹*Laboratoire Charles Coulomb (L2C),*

UMR 5221 CNRS-Université de Montpellier, F-34095 Montpellier, France

²*Institut Universitaire de France, F-75231 Paris, France*

³*International Centre for Theoretical Sciences,*

Tata Institute of Fundamental Research, Shivakote, Bengaluru 560089, India

(Dated: September 30, 2024)

CONTENTS

I. Fabrication of the microchannels	2
II. Visualization and tracking of the waves	3
III. Low-Reynolds-number instabilities	4
IV. Base flow profile of two co-flowing fluids in a rectangular channel	4
V. Accuracy of the interface position and interfacial velocity of the unperturbed interface	7
VI. Wave amplitude, confinement and critical rates of water	8
VII. Stability diagram	11
VIII. Comparison between miscible and immiscible fluids (Data from [1])	12
References	13

* Currently at Institute of Environmental Engineering, ETH Zurich, 8093, Zurich, Switzerland

† domenico.truzzolillo@umontpellier.fr

I. FABRICATION OF THE MICROCHANNELS

We generated the co-flow of deionized water and glycerol (Sigma Aldrich) and visualized their interface by pumping both fluids in polydimethylsiloxane (PDMS) microchannels. PDMS offers an easy fabrication and is optically transparent: it has thus been widely used for microfluidic applications, for the study of fluid dynamic instabilities and to tailor droplet or bubble generation [2–4]. The channels are formed via a mold obtained on a silicon wafer by means of photolithography [5]. A 9:1 w/w liquid mixture of silicone elastomer and curing agent (Sylgard 184) is poured on the mold and cured overnight at 70°C. The solid PDMS is then peeled from the mold and covalently attached to a microscope slide by means of plasma oxidation [6]. In order to inject and discharge the fluids, teflon microtubes (Scientific commodities Inc.) were plugged in the inlets and outlets by punching small holes in the PDMS, which constitutes the side and upper boundaries of the microchannels, while the bottom wall is the glass microscope slide.

We fabricated a Y-junction channel, as shown in Figure 1 of the main manuscript. The channel consists of a rectangular main duct ($H = 0.1$ mm, $W = 1,0.25$ mm), and two inlets having the same height and half of the width of the main duct, forming an angle of 43.6°. The two fluids flow parallel to each other and the interface is vertical, namely parallel to the gravity direction (\hat{z}). This configuration allows us to rule out the effect of density mismatch, at least in the first portion of the channel, where the two fluids stay in parallel co-flow and do not re-orient themselves to minimize gravitational energy. The whole system is visualized by means of optical microscopy. We use an inverted optical microscope (Leica DM IRB) equipped with a high-speed CCD camera (Phantom Miro M310) and one air objective (Leica, x10) . We recorded videos at 300 frames per second. The two fluids are pushed in the channel by means of two individual syringe pumps (Harvard Apparatus PHD 2000 Infusion) working at constant volumetric flow rates Q_G and Q_H , respectively. The use of two separate pumps allows one to impose separately the flow rates of the two fluids, and thus to characterize the coflow instability at different Reynolds number and independent values of Q_H , Q_G . Since glycerol is very hygroscopic and its viscosity is highly dependent on the amount of adsorbed water we have also measured its zero-shear viscosity at $T=25$ °C by continuous shear rheometry (AR 2000 rheometer - TA Instruments), in the range of shear rates $1 \text{ s}^{-1} \leq \dot{\gamma} \leq 100 \text{ s}^{-1}$ prior to its injection in the microchannel. We obtained a viscosity $\eta_2=(800 \pm 10)$ mPa s independent of the shear rate. After starting the injection or changing the flow rate, we wait several minutes for the system to reach a stationary state before acquiring data

in order to avoid transient effects due to the compliance of the injection apparatus and of the tubing in teflon.

II. VISUALIZATION AND TRACKING OF THE WAVES

The waves have been observed at their onset. Since we aim to study the steady state of the flow, we filmed the instability for several seconds. This allowed us to ascertain flow stationarity and to characterize the spatio-temporal behaviour of the waves, namely the dispersion of the wavelength λ , the phase speed v_{ph} and of the amplitude A of the waves, compatibly with our field of view (1.07 mm x 1.60 mm). From the videos we extracted the spatio-temporal averages and the temporal variances of all these observables. This has been done by means of a Python script (available at <https://zenodo.org/records/4001559>).

For the case of waves short enough so that several of them could be visualized simultaneously in the field of view, we extracted both λ and A by measuring the distance between adjacent local maxima and minima of the tracked interfaces in the x and y direction, respectively. As an example showing the accuracy of this image analysis routine, the positions of peaks and valleys of the disturbance are represented in Figure SM1. The phase velocity of the wave is obtained by tracking the position of either the maxima or the minima, and measuring the distance they travelled over a time set by two consecutive frames (3.3 ms). Mean values and experimental dispersions of the wavelength, the amplitude and the phase velocity of the propagating waves were obtained from the respective spatio-temporal variations over the duration of the videos (up to 120 s).

In other cases the interface developed a long wavelength disturbance, and only a single oscillation could be observed in the field of view (as shown for example in Figure 1-d). In such a case we could not measure the disturbance wavelength from the distance between two successive extrema and we used a different protocol: i) we first measured the phase velocity by tracking one wave front (maximum); ii) we calculated the wavelength by comparing the position of the aforementioned front at time $t = t_1$ with the successive one, taken at a later time t_2 . At t_2 the position of the first front, not visible any more in the field of view, can be calculated from its position at time t_1 , the elapsed time $\Delta t = t_2 - t_1$ and the phase velocity of the wave, the latter being spatially homogeneous within the resolution of our tracking method.

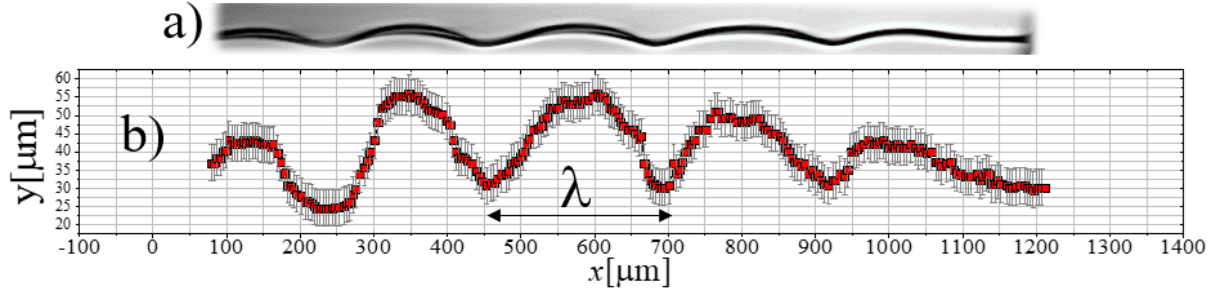


Figure SM1. **Instability visualization a):** The shear flow instability as visualized by optical microscopy ($Q_G = 18 \mu\text{l}/\text{min}$, $Q_H = 60 \mu\text{l}/\text{min}$). **Waveform characterization b):** The wave profile is measured by following the intensity minima resulting from the analysis of the images in gray scale (red points). Light gray bars represent the extent of the region where the intensity is different by more than 10% from the fluid background.

III. LOW-REYNOLDS-NUMBER INSTABILITIES

There is no turbulence in our experiments, in line with expectations from earlier theoretical work [7, 8]. To check whether turbulence sets in, we computed the Reynolds number for each pair of rates as $\bar{Re} = \frac{\bar{\rho}(Q_{H2O}+Q_{Gly})}{H\bar{\eta}}$ where $\bar{\rho} = \frac{Y\rho_1+(W-Y)\rho_2}{W}$ and $\bar{\eta} = \frac{Y\eta_1+(W-Y)\eta_2}{W}$. For the flow rates imposed to the two fluids in our experiments we obtain $0.013 \leq \bar{Re} \leq 0.254$ for the experiments performed in the wide channel ($W = 1 \text{ mm}$) and $0.015 \leq \bar{Re} \leq 0.135$ for those performed in the narrow channel ($W = 0.25 \text{ mm}$). These are ranges well below the critical Reynolds number $Re_{(cr)} > O(1000)$ at which turbulent flow sets in in rectangular ducts [9]. Moreover, even by considering the single flow of water in its effective duct of section $H \times Y$, the maximum Reynolds number attained would be $O(100)$, thus the flow would still be laminar, and a further comparison with the typical range of Re where Tollmien–Schlichting instabilities set in in two-phase flows ($O(10^4)$) excludes the latter mechanism as the one driving the observed interfacial destabilization [10]. We thus conclude that the observed waves are the result of a low Reynolds number linear instability created by viscosity stratification [7], followed by a nonlinear saturation.

IV. BASE FLOW PROFILE OF TWO CO-FLOWING FLUIDS IN A RECTANGULAR CHANNEL

We detail here the computation of the full base flow profile $U(y, z)$ of two co-flowing fluids in a rectangular channel, since it has not been explicitly detailed in literature. Following [11],

we consider a reference frame with the origin in the lower left-hand corner of the channel cross section. The fluids flow in the positive direction of the streamwise coordinate x , the channel covers the z (spanwise) direction in a range $0 < z < H$ and the vertical (wall-normal) direction y in a range $0 < y < W$. As sketched in Figure 1 of the main manuscript, $y = Y$ represents the position of the interface between the two fluids. With this choice of the reference frame, the base profile flow will be of type $\vec{V} = U(y, z)\hat{x}$.

For the sake of simplicity, we consider here the case of infinitely sharp interfaces, which is equivalent to consider a steady flow on time scales much shorter than that of diffusion. Therefore, we write $U(y, z)$ as a piecewise solution to Navier-Stokes' equations in the two fluid layers:

$$U(y, z) = \begin{cases} U_1(y, z) & \text{for } 0 < y < Y, 0 < z < H \\ U_2(y, z) & \text{for } Y < y < W, 0 < z < H. \end{cases} \quad (1)$$

Assuming the fluids to be incompressible, in each layer $U_i(y, z)$ will satisfy the streamwise component of the Navier-Stokes equations:

$$\eta_i \nabla^2 U_i(y, z) = \frac{\partial p}{\partial x}, \quad (2)$$

where η_i is the dynamic viscosity. Imposing no-slip boundary conditions at the left and right boundaries of the channel ($U_i(y, 0) = U_i(y, H) = 0$), the solution to Eq. 2 is known to take the Fourier form [11]:

$$U_i(y, z) = \frac{\partial p}{\partial x} \left\{ \frac{z(z-H)}{2\eta_i} + \sum_{m=1}^{\infty} \sin\left(\frac{m\pi z}{H}\right) \left[A_{i,m} \cosh\left(\frac{m\pi y}{H}\right) + B_{i,m} \sinh\left(\frac{m\pi y}{H}\right) \right] \right\}. \quad (3)$$

The coefficients $A_{i,m}$, $B_{i,m}$ are found by imposing the boundary conditions for the flow, namely no-slip conditions at the channel walls:

$$U_i(0, z) = U_i(W, z) = 0 \quad (4)$$

and the continuity of velocity and shear stress across the interface, i.e.:

$$U_1(Y, z) = U_2(Y, z), \quad (5)$$

$$\eta_1 \frac{\partial U_1(y, z)}{\partial y} = \eta_2 \frac{\partial U_2(y, z)}{\partial y}. \quad (6)$$

It is worth noting that since the shear stress is continuous across the interface, the derivative of the base velocity profile is not. Inserting Eqs. (4-6) in Eq. 3, one finds for the coefficients $A_{i,m}$, $B_{i,m}$:

$$A_{1,m} = \frac{K_m}{\eta_1}, \quad (7)$$

$$B_{1,m} = \frac{K_m}{\eta_1 C_m} \left\{ 2\eta_1 - S \cosh\left(\frac{Wm\pi}{H}\right) + D \left[\cosh\left(\frac{(W-2Y)m\pi}{H}\right) - 2\cosh\left(\frac{(W-Y)m\pi}{H}\right) \right] \right\}, \quad (8)$$

$$A_{2,m} = \frac{K_m}{\eta_2 C_m} \left\{ 2 \left[\eta_2 + D \cosh\left(\frac{Ym\pi}{H}\right) \right] \sinh\left(\frac{Wm\pi}{H}\right) - D \sinh\left(\frac{2Ym\pi}{H}\right) \right\}, \quad (9)$$

$$B_{2,m} = \frac{K_m}{\eta_2 C_m} \left\{ S - 2\cosh\left(\frac{Wm\pi}{H}\right) \left[\eta_2 + D \cosh\left(\frac{Ym\pi}{H}\right) \right] + D \cosh\left(\frac{2Ym\pi}{H}\right) \right\}, \quad (10)$$

with $S = \eta_1 + \eta_2$ and $D = \eta_1 - \eta_2$ the sum and the difference of the two viscosities, respectively. The coefficients K_m and C_m are given by

$$K_m = \frac{2H^2 [1 - (-1)^m]}{m^3 \pi^3}, \quad (11)$$

$$C_m = S \sinh\left(\frac{Wm\pi}{H}\right) + D \sinh\left(\frac{(W-2Y)m\pi}{H}\right). \quad (12)$$

The interface position Y can be measured experimentally, so that the velocity profile can be computed numerically. In order to do so, it is necessary to compute the pressure gradient $\frac{\partial p}{\partial x}$ as well, which is not known a priori: the experimental parameter are actually the flow rates of the fluids in the channel, Q_1 and Q_2 . However, the latter can be related to the pressure gradient, once the interface position is known. The total flow rate $Q = Q_1 + Q_2$ in the channel is simply the integral of the velocity profile:

$$Q = \int_0^W \int_0^H U(y,z) dy dz = \frac{\partial p}{\partial x} \int_0^W \int_0^H \tilde{U}(y,z) dy dz, \quad (13)$$

where we define $\tilde{U}(y,z) = U(y,z)/\frac{\partial p}{\partial x}$. Therefore, instead of computing $U(y,z)$ one can compute $\tilde{U}(y,z)$ first from Eq. 3 and integrate the latter in order to obtain the value of the pressure gradient from the flow rate Q . Moreover, the same procedure can be applied separately to the two fluids, since we deal with stationary flows and hence the same pressure gradient appears in the two $U_i(y,z)$ and the total flow rate is simply the sum of the two individual flow rates. One then finds:

$$Q_1 = \int_0^Y \int_0^H U_1(y,z) dy dz = \frac{\partial p}{\partial x} \int_0^Y \int_0^H \tilde{U}_1(y,z) dy dz, \quad (14)$$

$$Q_2 = \int_Y^W \int_0^H U_2(y,z) dy dz = \frac{\partial p}{\partial x} \int_Y^W \int_0^H \tilde{U}_2(y,z) dy dz. \quad (15)$$

Equation 13 and Eqs. (14-15) allow one to compute the pressure gradient in two independent ways and thus to further verify the accuracy of the analysis of the experimental data.

V. ACCURACY OF THE INTERFACE POSITION AND INTERFACIAL VELOCITY OF THE UNPERTURBED INTERFACE

Once the viscosities of the co-flowing fluids are given, the characteristic quantities defining of the flow profile are the two imposed flow rates (Q_H, Q_G), the position of the interface (Y) and the pressure gradient ($\frac{\partial p}{\partial x}$) in the stream wise direction. Out of the four, only two are indeed needed to fully compute the flow, as the other two are calculated accordingly (see Section IV). Since experimentally one imposes the flow rates of the fluids, these are the ones that we choose to fix for the computation. The position of the interface is known from the experiments as well, and can be used to cross check the precision of the computation. In detail: the interface position Y is obtained numerically as the one for which the pressure gradient is homogeneous throughout the whole channel, given the two flow rates. Comparing the obtained value of Y with the one which is measured experimentally allows us to evaluate the agreement between the experiments and the numerical solution for the base profile (Fig. SM2), and successively therefore the precision in computing the base flow velocity at the interface (shown in Fig. SM3). The sources of error are both computational and experimental. i) Since the velocity profile is expressed as a Fourier series, higher order terms will always be discarded for computational efficiency, as we typically retain between 5 to 7 harmonics. ii) The experiments are affected by noise and measurement uncertainties stemming from several sources. In particular the imposed flow rates are affected by the stability of the syringe pumps and that of the PDMS, which is likely to slightly deform under the action of the pressure due to the flow [12]. Comparing the value of Y obtained from the experiments to that from the numerical calculation of the base flow allows for evaluating the effect of the resulting noise from all such sources. Figure SM2 displays this comparison for the representative case of water flowing at different Q_H parallel to glycerol flowing at $Q_G = 15 \mu\text{l}/\text{min}$. The discrepancy, due to all sources of noise in the experiments and numerical solutions, is less than 10% of the values (bars in Fig. SM2). Similarly, one can evaluate the uncertainty on the computed base velocity profile by using Y as an input parameter for the analytical solution (together with one of the two flow rates, such as for example Q_H) and by comparing the results obtained using either the experimental value of Y or the one retrieved from the numerical solution once the flow rates are fixed, namely the filled symbols and the empty ones in Fig. SM2. Using these two values for Y gives slightly different results for the other quantities describing the flow such as the interface velocity $U(y = Y)$. Figure SM3 shows $U(y = Y)$ obtained by fixing the interface position to the

one measured in experiments according to the protocol described in section II. The so-obtained values of $U(y = Y)$ differ from those obtained by imposing the position Y obtained analytically by fixing the two flow rates (Q_H, Q_G) by less than 5%. The values of $U(y = Y)$ have been subtracted to the phase velocity of the waves in the lab frame to obtain the phase velocity in the frame of the unperturbed interface.

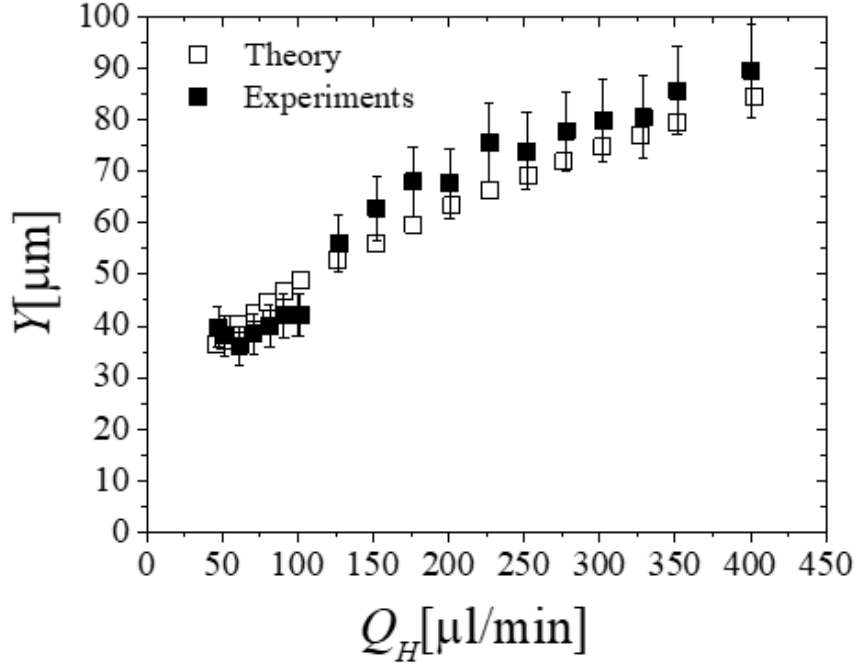


Figure SM2. Comparison between the measured interface position Y (black filled symbols) and the one obtained from the numerical solution of the base profile (open symbols) as a function of Q_H , for water flowing parallel to glycerol with $Q_G = 15 \mu\text{l}/\text{min}$ in the channel with $W = 1$. The bars on the experimental values represent a 10% relative uncertainty.

VI. WAVE AMPLITUDE, CONFINEMENT AND CRITICAL RATES OF WATER

Figure SM4-a shows the amplitude A of the instabilities for the same pair of rates (Q_G, Q_H) as in Fig. 2 of the main manuscript. Similarly to the phase speed, the amplitude shows two regimes with a rapid increase followed by a nearly constant plateau for increasing Q_H , with Q_G determining the value of the plateau, which increases for increasing Q_G . The two regimes observed for the amplitude A of the waves turns out to be related to the type of waves. All the waves belonging to the C -branches are characterized by the same amplitude, while for the CD -waves the amplitude

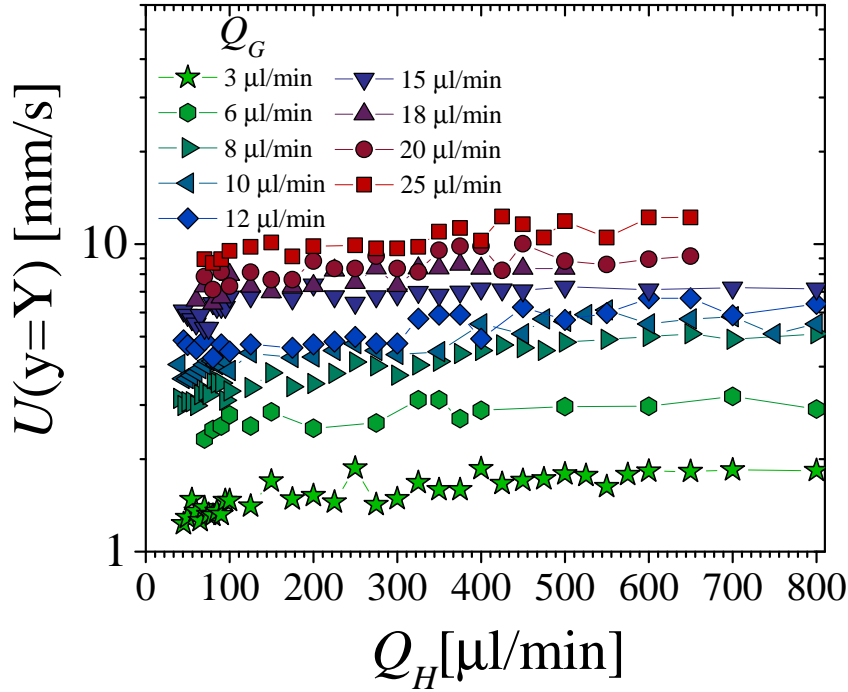


Figure SM3. Base flow velocity at the boundary between the two fluids $U(y = Y)$ obtained by measuring the interface position Y and fixing the flow rate of water Q_H to the nominal one.

varies significantly upon changing Q_H . To characterize the y -range of this variation and hence the distance from the wall ($y = 0$) at which the transition between C and CD waves occurs, we inspected the behavior of the amplitude in function of the position of the unperturbed interface Y , and fitted $A(Y)$ with a phenomenological exponential function $A(y) = A_0 \{1 - \exp[-(Y - Y_0)/\xi]\}$, where ξ is a characteristic length characterizing the transition from variable amplitude to constant amplitude (A_0), and Y_0 the critical position of the interface above which the instability emerges. When properly rescaled (Figure SM4-b), the amplitudes collapse on the same master curve, with all the points belonging to the C -branch (colored points) appearing for interface positions such that $(Y - Y_0) \gtrsim 2\xi$ while CD -branches (gray points) correspond to smaller Y values, where the amplitude goes rapidly to zero for decreasing Q_H (and Y). We observe that the characteristic length ξ (Figure SM4-c) does not show any remarkable change in the range $8 \mu\text{l}/\text{min} < Q_{Gly} \leq 25 \mu\text{l}/\text{min}$ where we observe the C -branch. By contrast, the transition to the D -branch for the lowest rate of glycerol ($Q_G = 3$ and $6 \mu\text{l}/\text{min}$) is characterized by a significant increase of ξ , pointing to a much larger range over which the amplitude is affected by the interface position. We interpret

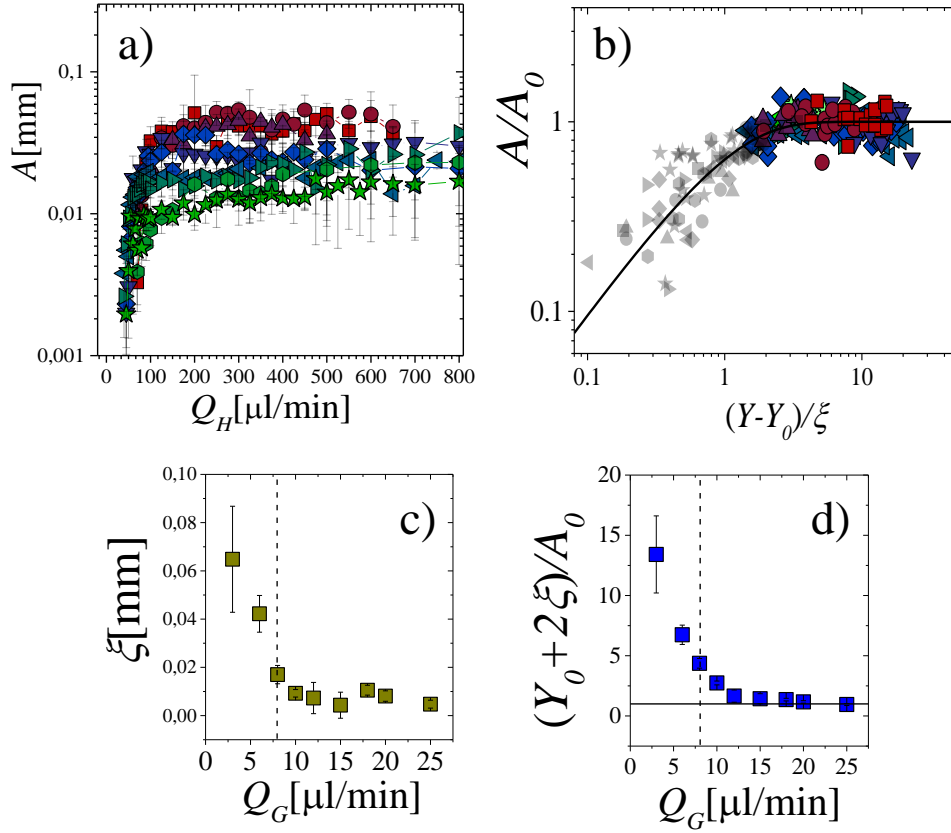


Figure SM4. **a)**: Amplitude A of the waves as a function of Q_H for different flow rates of glycerol Q_G . The color code and the symbols are the same as in Fig. 2 of the main text and Fig. SM3. **b)**: Normalized amplitude vs rescaled interface position following the auxiliary function (see text) used to fit $A(Y)$. **c)**: Characteristic length ξ . **d)**: Normalized distance $(Y_0 + 2\xi)/A_0$ from the wall at $y = 0$ at which the transition between rapidly varying amplitudes and constant amplitude occurs. The horizontal solid line correspond to $(Y_0 + 2\xi)/A_0 = 1$. The vertical dashed lines in panels **c)** and **d)** mark $Q_G = 8 \mu\text{l}/\text{min}$, i.e. the lowest flow rate of glycerol at which capillary waves (C -branch) have been observed.

this as a larger impact of the confinement on the flow. To further corroborate this hypothesis, we plot in Fig. SM4-d the absolute position of the boundary between the two regimes, $Y_0 + 2\xi$, normalized to the amplitude A_0 far from the wall. Interestingly, we find that $(Y_0 + 2\xi)/A_0 \rightarrow 1$ for large Q_G where the tension is large and the capillary branch is the most extended. This points to waves that turn from capillary ones (C) to CD -type only when the unperturbed interface Y goes below the wave amplitude observed far from the wall at $y = 0$, i.e. when the wave is physically compressed by the wall. This suggests, once more, that ξ is indeed dictated by confinement.

Wall confinement therefore affects wave propagation on larger spatial scales (larger ξ) for lower Q_G , where the effective tension is lower but the system is also closer to the stability region of the two-liquid flow, hampering the onset of capillary wave propagation. We further employed the

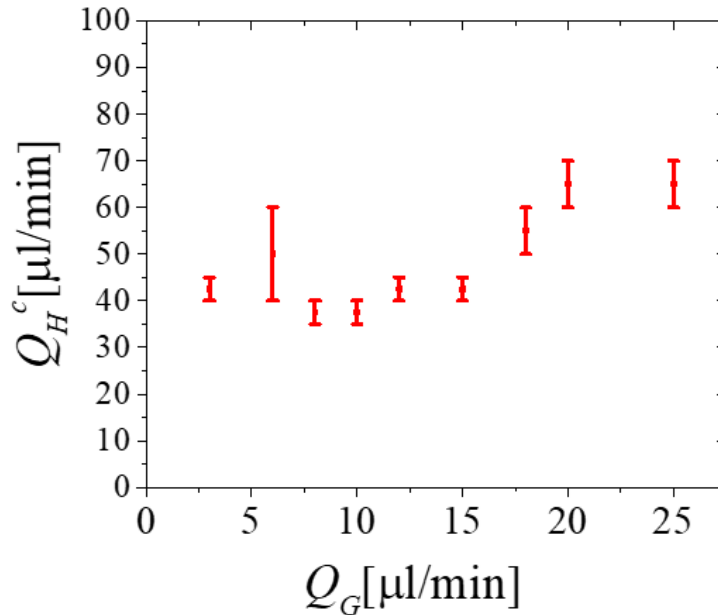


Figure SM5. Critical flow rate of water $Q_H^c(Q_G)$ marking the boundary between unstable and stable flows (see "Stable" region in figure SM6) in the channel with $W = 1$ mm. The bars are the intervals defined respectively by the lowest rates of water at which a finite wave amplitude could be observed (upper bound) and the highest probed value of Q_H at which the instability could not be observed anymore (lower bound).

amplitude $A(Q_H, Q_G)$ to define the critical flow rate of water Q_H^c for each flow rate of glycerol, above which the shear flow instability appears. We define it as the center of the intervals reported in figure SM5. For each value of Q_G , the boundaries of the intervals are defined respectively as the lowest rates of water at which a finite wave amplitude could be resolved by optical microscopy (upper bound) and the probed value of Q_H at which the instability could not be observed anymore (lower bound).

VII. STABILITY DIAGRAM

Figure SM6 shows the stability diagram in the Q_G - Q_H plane for water and glycerol injected in the wide channel ($W=1$ mm). All points mark the pair of rates at which the interfacial waves appeared and could be tracked. The dashed line indicates the boundaries between capillary waves

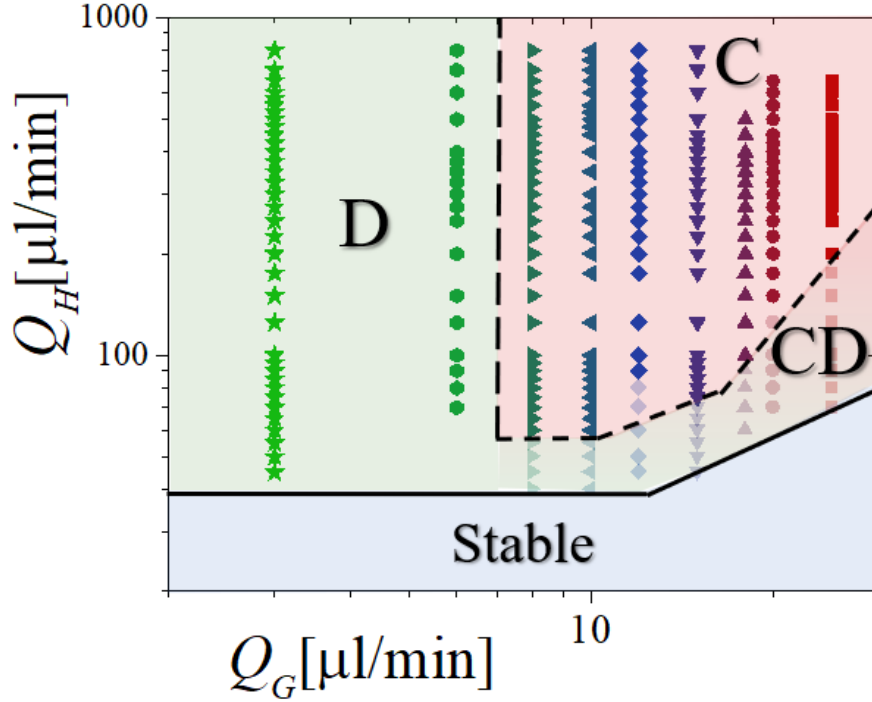


Figure SM6. Stability diagram in the plane defined by the rate of the two co-flowing fluids (Q_G , Q_H) for the instability observed in the channel with $W = 1$ mm. Same symbols and color code as in Fig. SM3.

(C), the inertial regime (D), and the transition zone (CD) that eventually terminates (full line) in the stable region of the diagram, where the fluid-fluid interface is stable.

VIII. COMPARISON BETWEEN MISCIBLE AND IMMISCIBLE FLUIDS (DATA FROM [1])

We compare here the our data obtained for water and glycerol in the wide channel ($W = 1$) with those reported by Hu and Cubaud in [1] for ethanol ($\eta_E = 1.08$ mPa s, $\rho_E = 780$ kg/m³) and silicon oil ($\eta_S = 485$ mPa s, $\rho_S = 970$ kg/m³) injected in a channel with squared section $H \times W = 0.25 \times 0.25$ mm. The equilibrium interfacial tension between the two fluids studied in [1] is $\Gamma = 1.09$ mN/m. It's worth noting that the compared pairs of fluids have viscosity contrasts $\eta_S/\eta_E = 449$ and $\eta_G/\eta_H = 898$ of the same order of magnitude and that the two immiscible fluids have an interfacial tension close to the maximum tension measured in our experiments for water and glycerol ($\Gamma_e = 2.3$ mN/m for $Q_G = 25$ μl/min). Densities and interfacial tension allow us to compute the prefactor α (see main manuscript) for silicon oil and ethanol and compare their dispersion $k(\omega/\alpha)$ to the one measured for water and glycerol. This is shown in Figure SM7:

the very good overlap between the two distinct sets of data for both capillary waves and inertial regime points to a very general behavior for these shear flow instability, with capillary waves dominating at low wavenumbers and with a limiting upper value for k dominated by dissipation and confinement. The overlap between the dispersion of waves observed in pairs of immiscible fluids with the one measured in fully miscible ones, further support the importance of interfacial stresses in miscible fluids over short diffusion times.

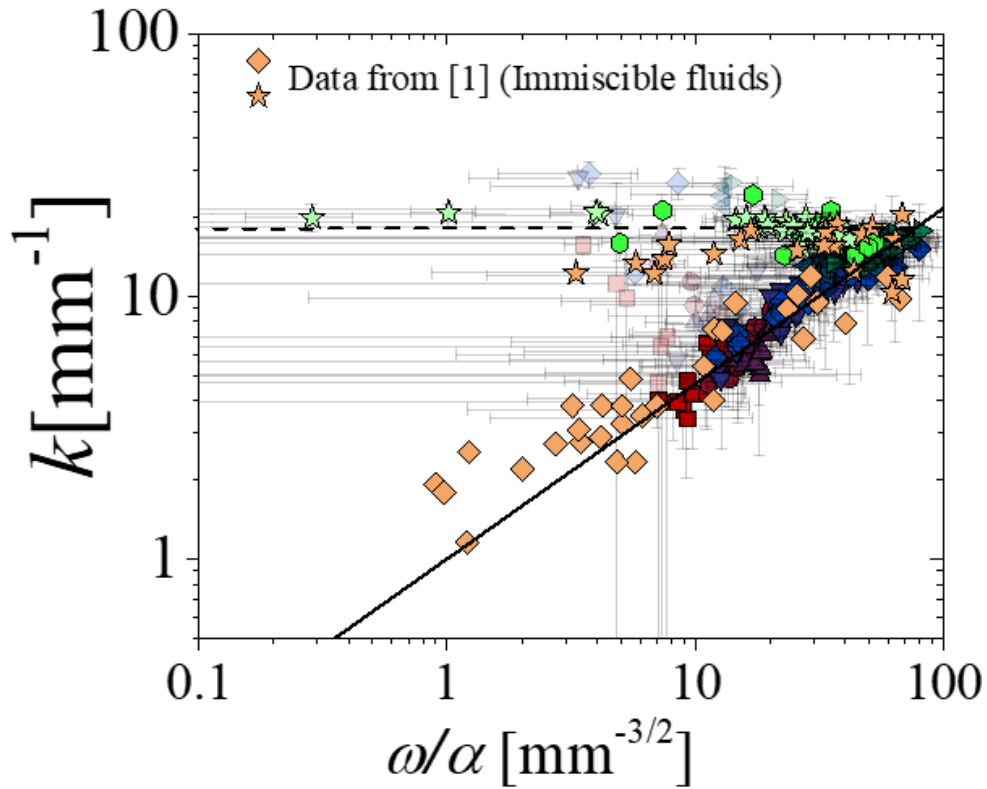


Figure SM7. Dispersion relation k vs ω/α for the waves observed in the wide channel ($W = 1$ mm) for water and glycerol in the present work. Symbols are the same as in Fig. 4-a of the main manuscript. Orange points correspond to the capillary branch (diamonds) and inertial regime (stars) reported in ref. [1] (ref. [7] of the main manuscript) for co-flowing ethanol and silicon oil, two immiscible fluids.

[1] X. Hu and T. Cubaud, Viscous Wave Breaking and Ligament Formation in Microfluidic Systems, Phys. Rev. Lett. **121**, 044502 (2018).

- [2] P. Guillot, P. Panizza, J.-B. Salmon, M. Joanicot, A. Colin, C.-H. Bruneau, and T. Colin, Viscosimeter on a Microfluidic Chip, *Langmuir* **22**, 6438 (2006).
- [3] T. Cubaud and T. G. Mason, High-viscosity fluid threads in weakly diffusive microfluidic systems, *New J. Phys.* **11**, 075029 (2009).
- [4] M. De Menech, P. Garstecki, F. Jousse, and H. A. Stone, Transition from squeezing to dripping in a microfluidic T-shaped junction, *J. Fluid Mech.* **595**, 141 (2008).
- [5] P. Tabeling, *Introduction to Microfluidics*, 2nd ed. (Oxford University PressOxford, 2023).
- [6] J. Friend and L. Yeo, Fabrication of microfluidic devices using polydimethylsiloxane, *Biomicrofluidics* **4**, 026502 (2010).
- [7] R. Govindarajan and K. C. Sahu, Instabilities in Viscosity-Stratified Flow, *Annu. Rev. Fluid Mech.* **46**, 331 (2014).
- [8] R. Govindarajan, Effect of miscibility on the linear instability of two-fluid channel flow, *International Journal of Multiphase Flow* **30**, 1177 (2004).
- [9] I. Tosun, D. Uner, and C. Ozgen, Critical Reynolds number for Newtonian flow in rectangular ducts, *Ind. Eng. Chem. Res.* **27**, 1955 (1988).
- [10] K. C. Sahu and R. Govindarajan, Linear stability analysis and direct numerical simulation of two-layer channel flow, *J. Fluid Mech.* **798**, 889 (2016).
- [11] P. J. Stiles and D. F. Fletcher, Hydrodynamic control of the interface between two liquids flowing through a horizontal or vertical microchannel, *Lab Chip* **4**, 121 (2004).
- [12] H. Stone, A. Stroock, and A. Ajdari, Engineering Flows in Small Devices: Microfluidics Toward a Lab-on-a-Chip, *Annu. Rev. Fluid Mech.* **36**, 381 (2004).